

Supporting Information

Role of defect density in TiO_x protective layer of n -Si photoanode for efficient photoelectrochemical water splitting

Songwoung Hong, Woo Lee, Yun Jeong Hwang, Seungwoo Song, Seungwook Choi, Hyun Rhu, Jeong Hyun Shim, Ansoon Kim*

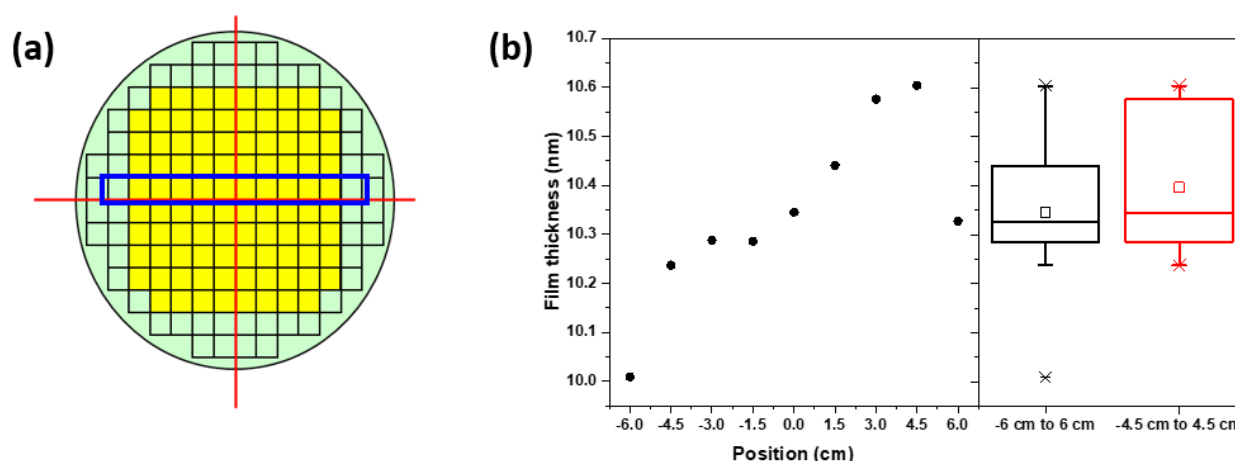


Fig. S1. (a) Schematic illustration of 6-inch wafer diced for photoanode experiments. The yellow region represents selected homogeneous region. The blue region represents where the TiO_2 film thickness distribution was examined. (b) Spectroscopic ellipsometry result for the TiO_2 film thickness. Box plot for the TiO_2 thickness distribution was obtained from the blue region in (a) of 6-inch wafer with 10 nm TiO_x overlayer. As the thickness at -6 cm apart from the center of wafer is an outlier, we selected yellow region for photoanode experiments.

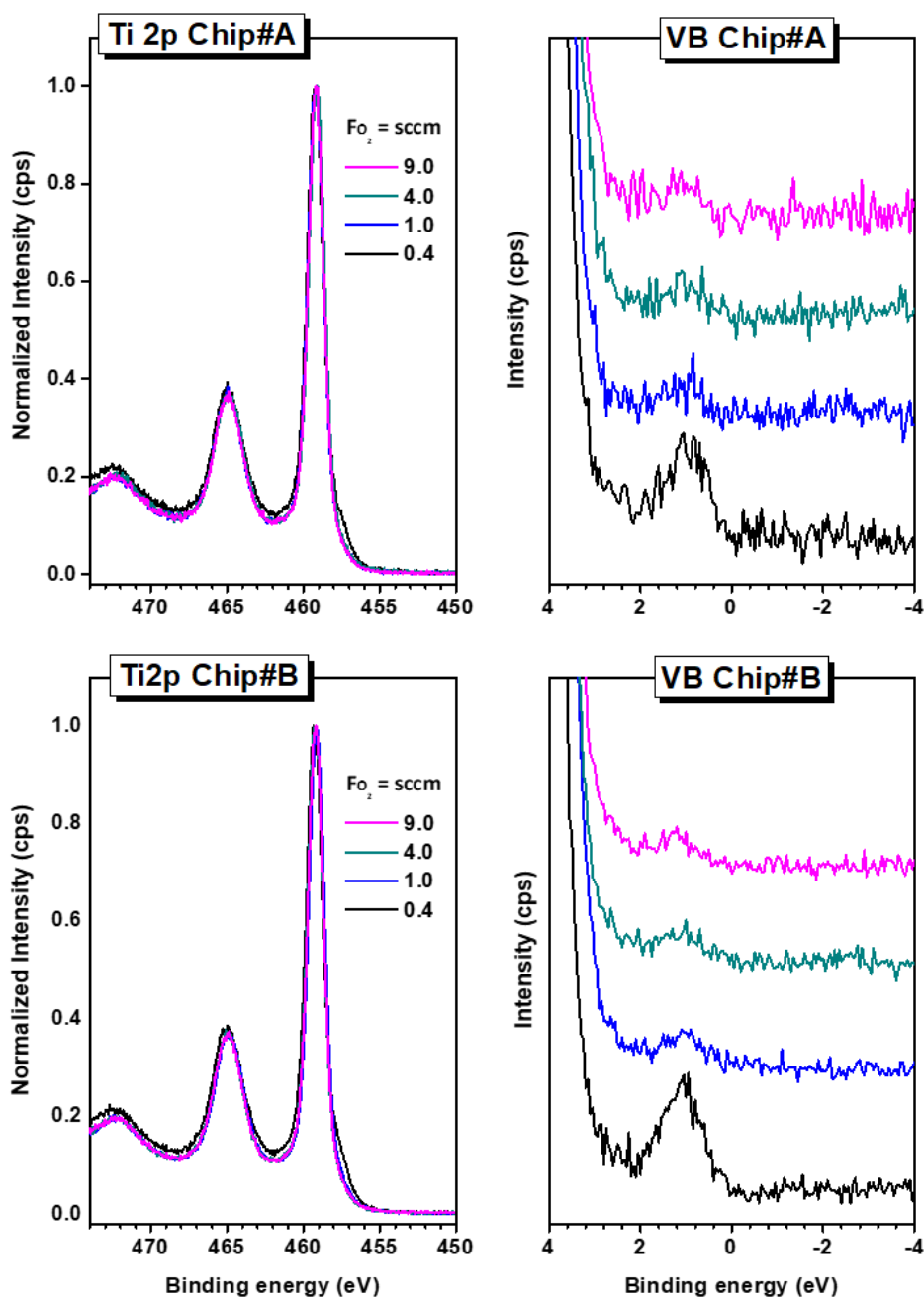


Fig. S2. The comparison of Ti 2p and valence band spectra between sample locations within yellow region in a wafer. The results confirm the reproducibility in the quantity of Ti^{3+} state and defect-related midgap states of TiO_x within identical sample lot.

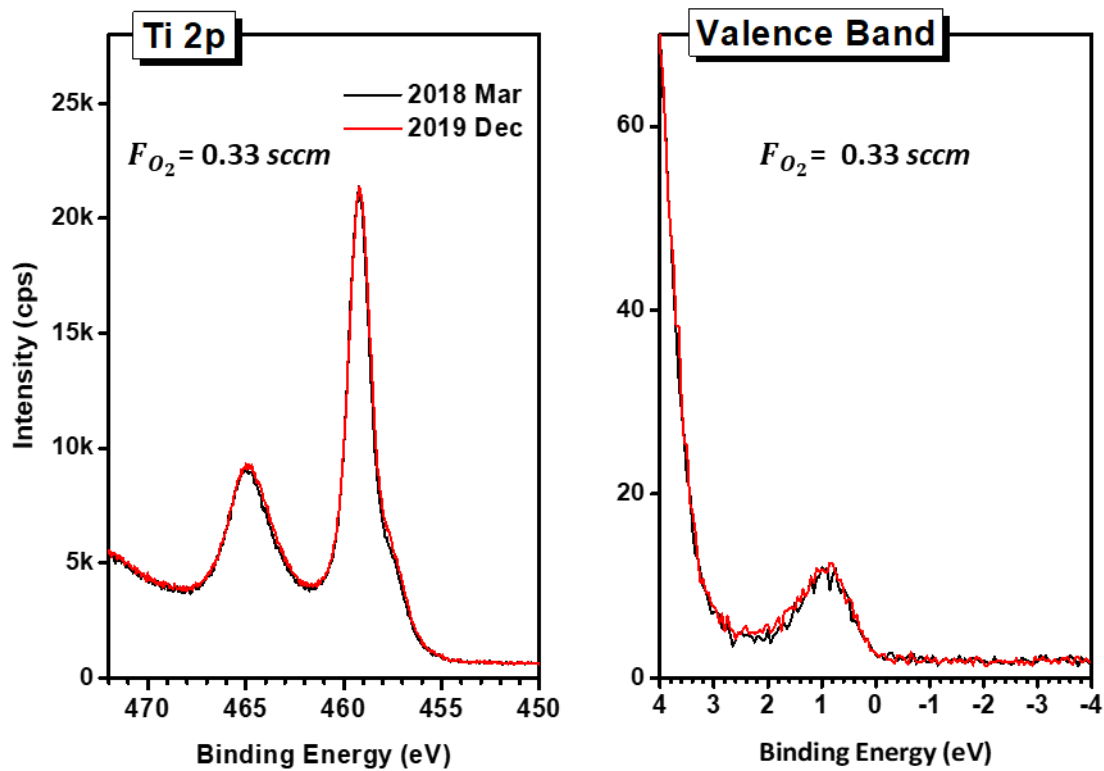


Fig. S3. The comparison of Ti 2p and valence band spectra between 0.33 sccm-TiO_x samples fabricated in Dec, 2019 (red) and Mar, 2018 (black). Both samples demonstrated a great reproducibility even though they are fabricated at 18 months apart.

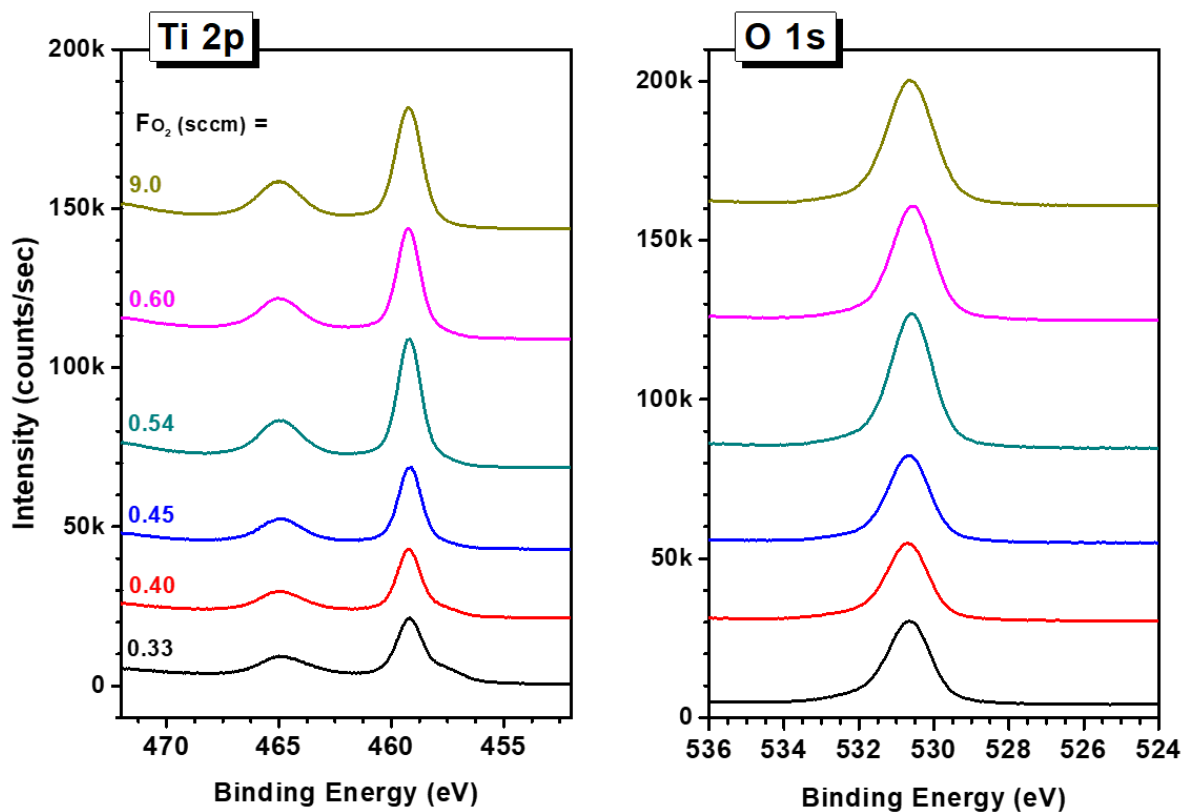


Fig. S4. XPS spectra of TiO_x films deposited with individual oxygen flow during the sputtering. The peak intensities of Ti 2p and O 1s core level were used for the stoichiometry of TiO_x , presented in Table S1.

Table S1. Stoichiometry of TiO_x films deposited with individual oxygen flow during the sputtering. The stoichiometry was determined by the composition analysis based on core level spectra of Ti 2p and O 1s measured by XPS (Fig. S4). For the composition analysis, we used relative sensitivity factor for each core level provided by XPS manufacturer.

Oxygen flow (sccm)	0.33	0.40	0.45	0.54	0.60	9.0
Stoichiometry of TiO_x layer	$\text{TiO}_{1.94 \pm 0.02}$	$\text{TiO}_{1.95 \pm 0.02}$	$\text{TiO}_{1.96 \pm 0.02}$	$\text{TiO}_{1.98 \pm 0.02}$	$\text{TiO}_{1.99 \pm 0.02}$	$\text{TiO}_{2.00 \pm 0.01}$

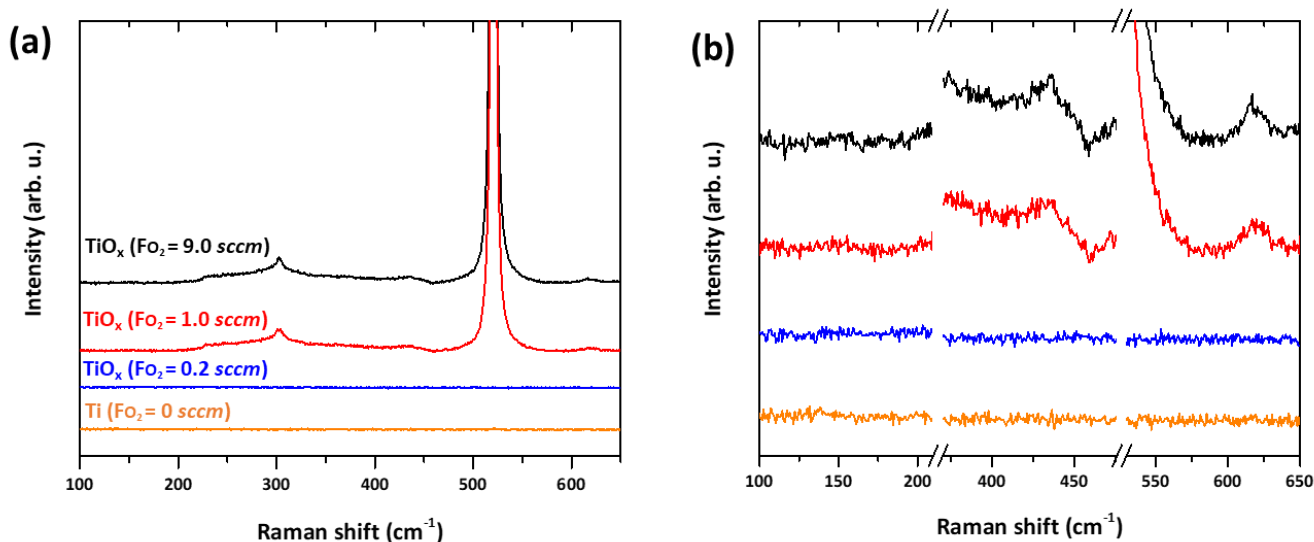


Fig. S5. Raman spectra of TiO_x films deposited under varying oxygen flow (0-9 *sccm*). (a) Full range Raman spectra of 100-650 cm^{-1} and (b) broken plot of (a) to clarify the presence of Raman vibrations for crystalline TiO_2 phase.

It was reported that Raman active modes of rutile TiO_2 were observed at 143 (B_{1g}), 449 (E_g) and 611 cm^{-1} (A_{1g}).¹ On the other hand, anatase TiO_2 showed characteristic peak at 144 (E_g), 397 (B_{1g}), 516 (A_{1g} , B_{1g}), 639 cm^{-1} (E_g).¹ The absence of characteristic Raman bands for crystalline TiO_2 phase suggests that the deposited TiO_x film is amorphous. The peaks measured at 302 cm^{-1} , 433 cm^{-1} and 618 cm^{-1} are associated with two-phonon Raman scattering of transverse acoustic mode (TA) at X critical point, scattering involving phonons along Σ , and a combination of TA and transverse optical (TO) phonons in the Σ direction, respectively.^{2,3}

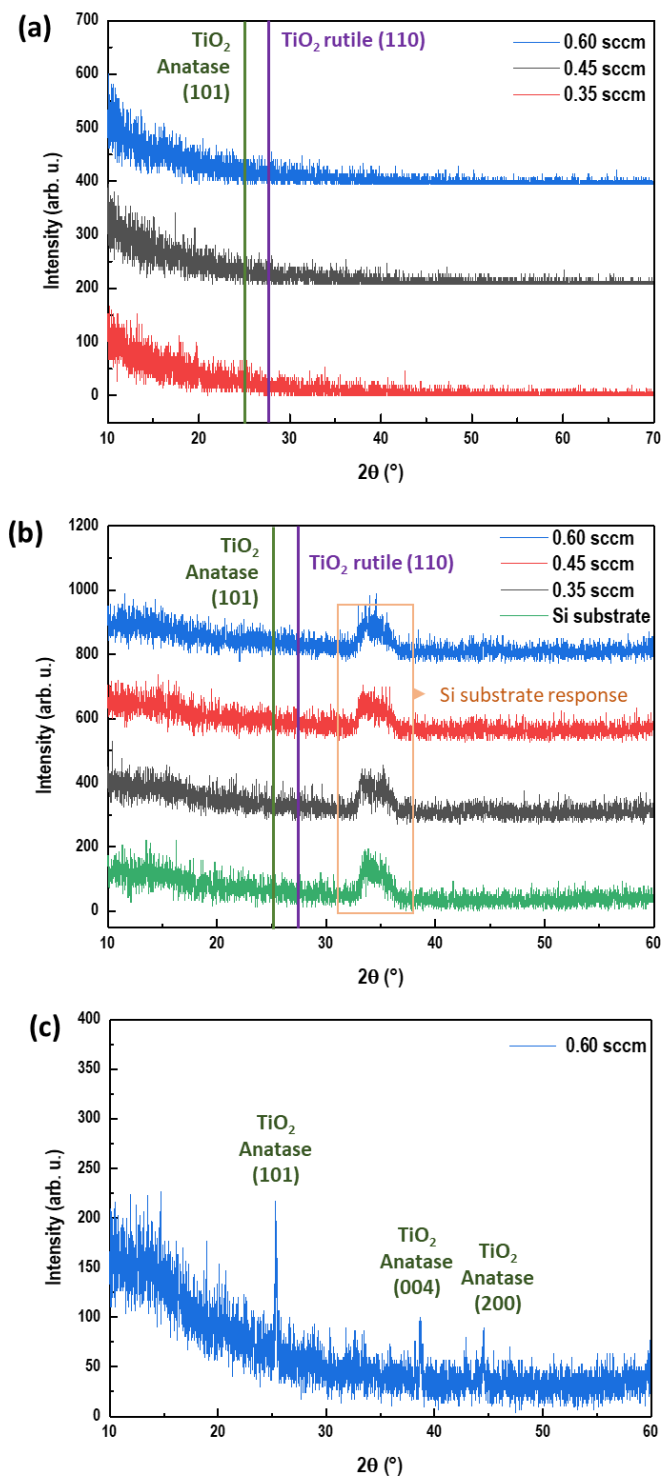


Fig. S6. Crystallinity of 50 nm TiO_x films deposited under varying oxygen flow (0.35 ~ 0.60 *sccm*). (a) Grazing incidence X-ray diffraction (GIXRD) and (b) conventional $\theta/2\theta$ mode XRD of the 50 nm TiO_x films. All samples exhibited no characteristic crystalline TiO_2 phase, which suggests the deposited TiO_x film is amorphous. (c) Conventional $\theta/2\theta$ mode XRD of 50 nm 0.6 sccm - TiO_x film annealed at 500°C for 1 h under Ar in tube furnace to form anatase crystalline TiO_2 phase.

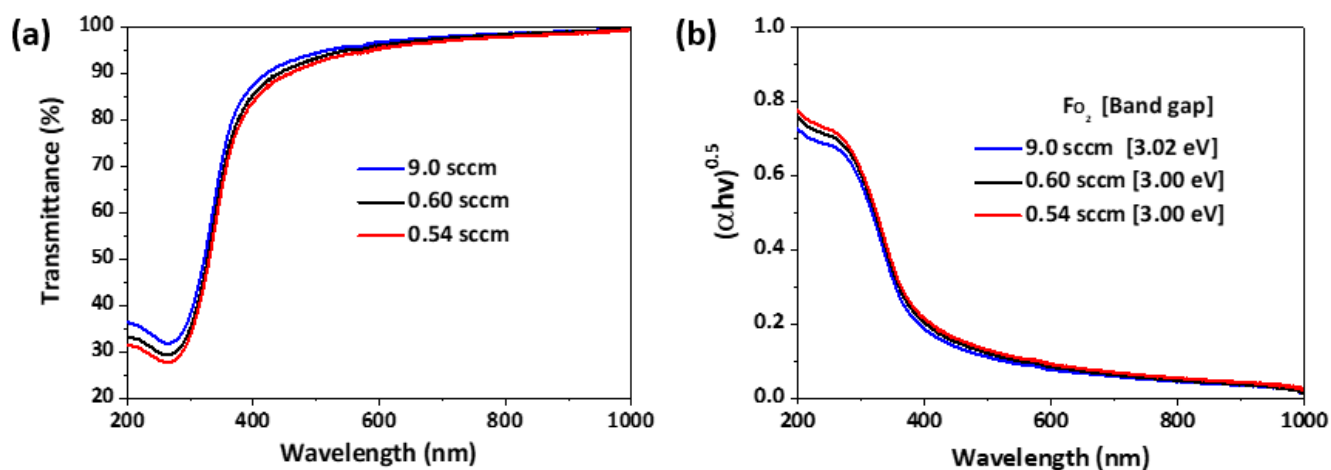


Fig. S7. Optical properties of 10 nm-thick TiO_x films deposited on quartz substrate with various oxygen flow.

(a) Transmittance and (b) Tauc plots of each TiO_x film.

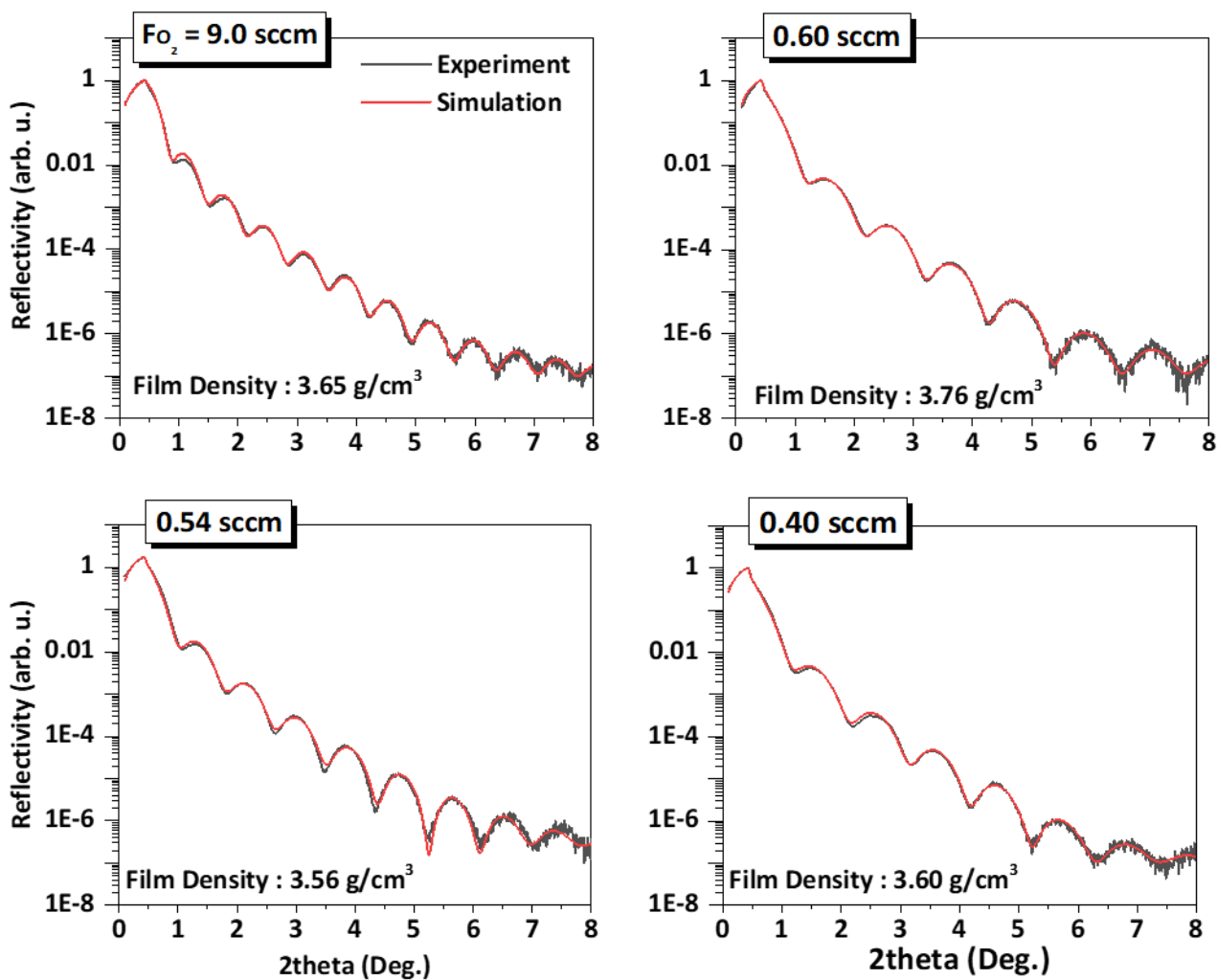


Fig. S8. Correlation between deposition condition and film density of various TiO_x films: X-ray Reflectivity (XRR) pattern and simulated film density. All the films represent the film density ranging from 3.56 g/cm^3 to 3.76 g/cm^3 , which are comparable to previously reported density, approximately $3.25\text{--}3.68 \text{ g/cm}^3$, of TiO_2 film⁴⁻⁶. There is no correlation between the film density and the oxygen flow. To determine the best fit of the measured XRR spectrum, we consider a two-layer model including interfacial native SiO_x less than 1 nm and TiO_x to investigate the density and thickness of deposited films. In addition, the simulated XRR data further supported that the thickness of deposited films is approximately 10 nm.

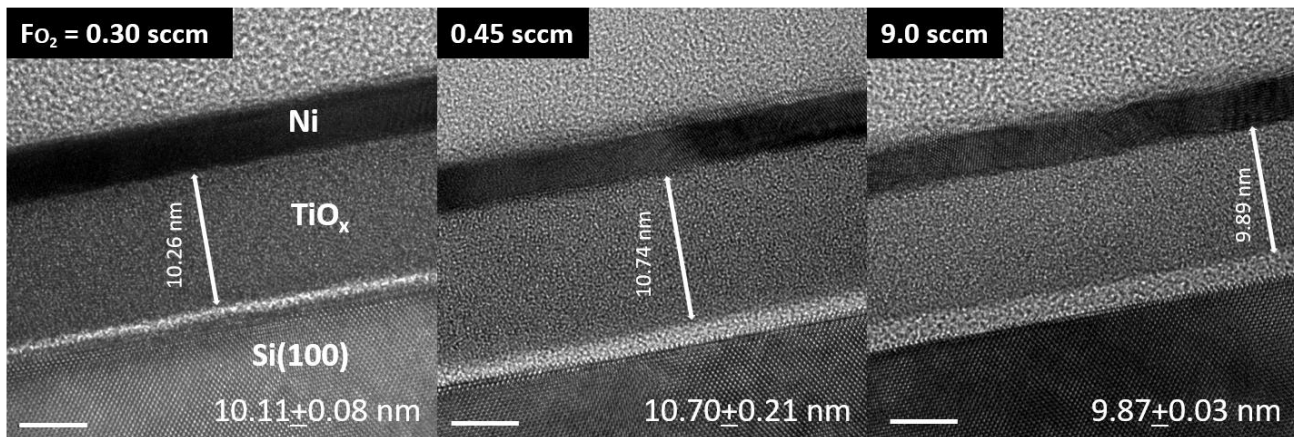


Fig. S9. Cross-sectional TEM images of *n*-Si/TiO_x/Ni photoanode fabricated with individual oxygen flow (scale bar = 5 nm). The mean and standard deviation of TiO_x thickness was obtained from nine independent analysis, and shown as caption at the bottom of figure.

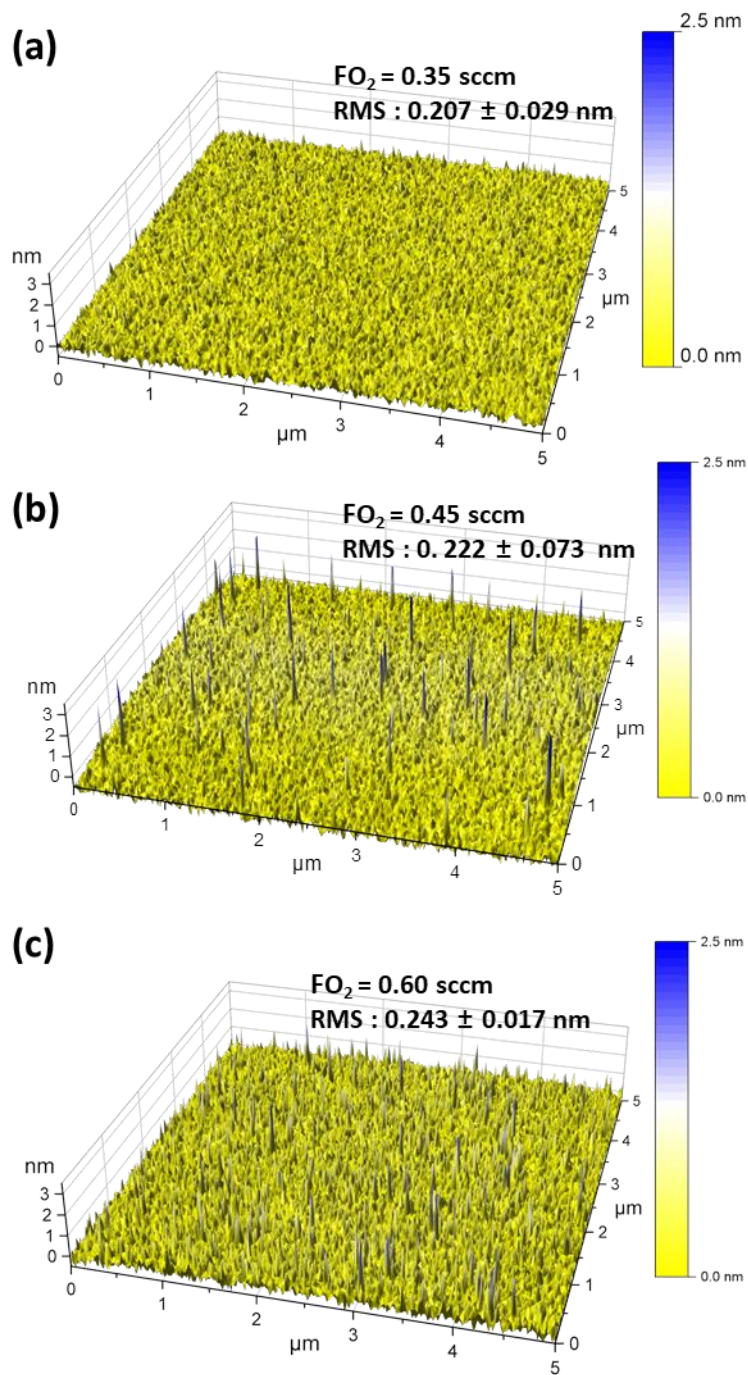


Fig. S10. Atomic force microscopy (AFM) morphology images of n -Si/TiO_x/Ni photoanode examined in Figs. 1 and 2. The O₂ flow for the TiO_x layers is (a) 0.35, (b) 0.45 and (c) 0.60 sccm. RMS roughness is indicated in the figures. The standard deviation was calculated by multiple measurements on different surface area and sample.

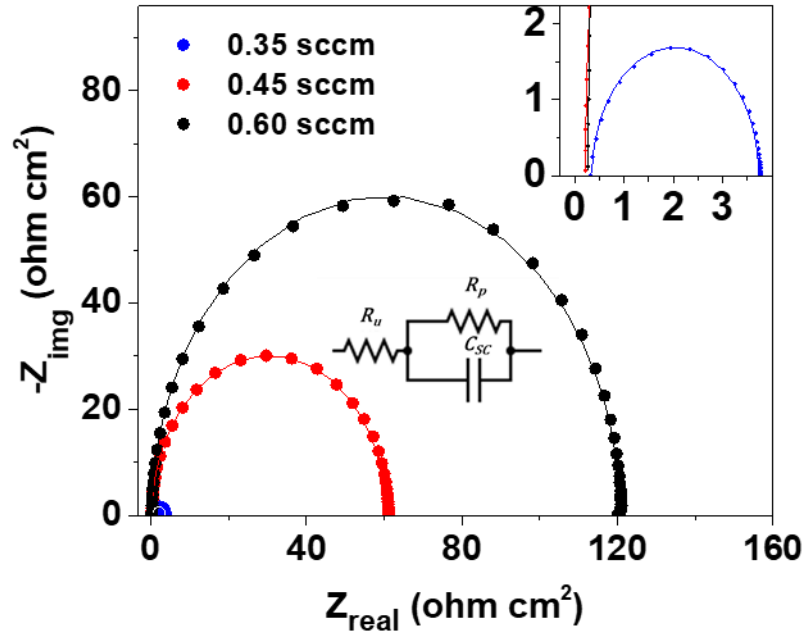


Fig. S11. Impedance spectroscopy (IS) analysis of 10 nm-thick TiO_x films and their equivalent circuits. TiO_x films (10 nm) and Ni co-catalyst layer (3.3 nm) were deposited on p^+ -Si wafer ($0.004 \Omega\text{-cm}$) to examine the electrical properties of only TiO_x films while excluding the influence of the substrate. In addition, ohmic contacted front metal contacts by using thermal evaporated Al (about 500 nm) were formed on TiO_x/Ni , while back ohmic contacts were formed using In-Ga eutectic, to eliminate the influence of electrolyte as well. The device structure is In-Ga eutectic alloy/ p^+ -Si wafer ($0.004 \Omega\text{-cm}$)/ TiO_x (10 nm)/Ni (3.3 nm)/Al. In order to quantify the impact of defect concentration on electrical properties, Nyquist plots were fitted to simplified Randle cells (inset of Fig. S11). The simplified Randles cell represents series resistance (R_u), charge transfer resistance (R_p), and space charge capacitance (C_{SC}) of the TiO_x of the solid-state device. The semicircle response of TiO_x deposited in 0.60 *sccm* demonstrated the largest semicircle, while the 0.35 *sccm* sample showed the smallest. The impedance spectroscopy was performed at a DC bias of 0 V by sweeping between 1 MHz and 0.2 Hz and using a sine-wave amplitude of 5.0 mV.

Table S2. Summary of equivalent circuit fitting from the impedance spectroscopy (Fig. S11) of various TiO_x film.

Oxygen flow (<i>sccm</i>)	R_p (ohm·cm ²)	R_u (ohm·cm ²)	C_{SC} (μF·cm ⁻²)	Specific conductance (nS·cm ⁻¹)
0.35	3.4	0.344	3.91	219.8
0.45	60.2	0.211	2.91	16.7
0.60	120.3	0.266	2.41	10.0

In this analysis, all three samples demonstrated very small R_u ($\ll 0.35 \Omega \text{ cm}^2$) since the R_u arises from the metal to semiconductor junction, not from a solution to semiconductor junction. The primary contribution to C_{SC} is space charge capacitance of the TiO_x rather than double-layer capacitance due to the existence of metal-semiconductor junction. In comparison with TiO_x deposited in 0.60 and 0.45 *sccm*, the 0.35 *sccm* sample showed dramatically decreased charge transfer resistance, which demonstrates the direct correlation between the defect concentration and the conductivity of TiO_x films. In addition to the charge transfer resistance, the TiO_x with the highest defect concentration showed higher film capacitance, which likely represents the increased defect concentration of the TiO_x films⁷. Specific conductance was calculated with following equation.

$$\text{Specific conductance} = \frac{\varepsilon_{TiO_x} \varepsilon_0}{R_p C_{SC}}$$

where ε_{TiO_x} is dielectric constant of TiO_x and ε_0 is vacuum permittivity.

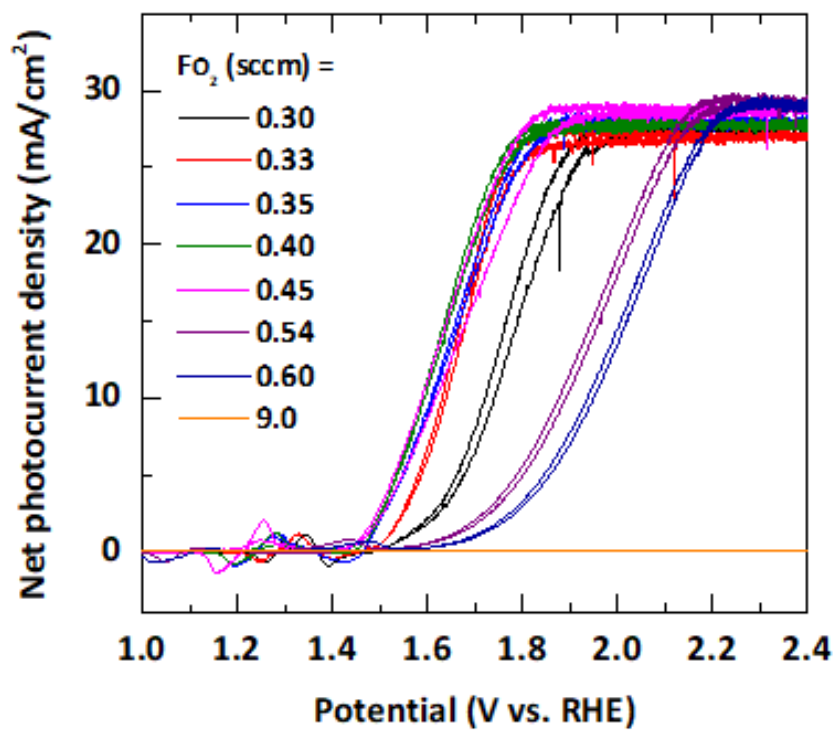


Fig. S12. Stirred cyclic voltammetry of TiO_x protected *n*-Si photoanodes plotted as net photocurrent vs. potential depicted in Fig. 2c. The net photocurrent density was determined by subtracting the dark current density from the total saturation photocurrent density.

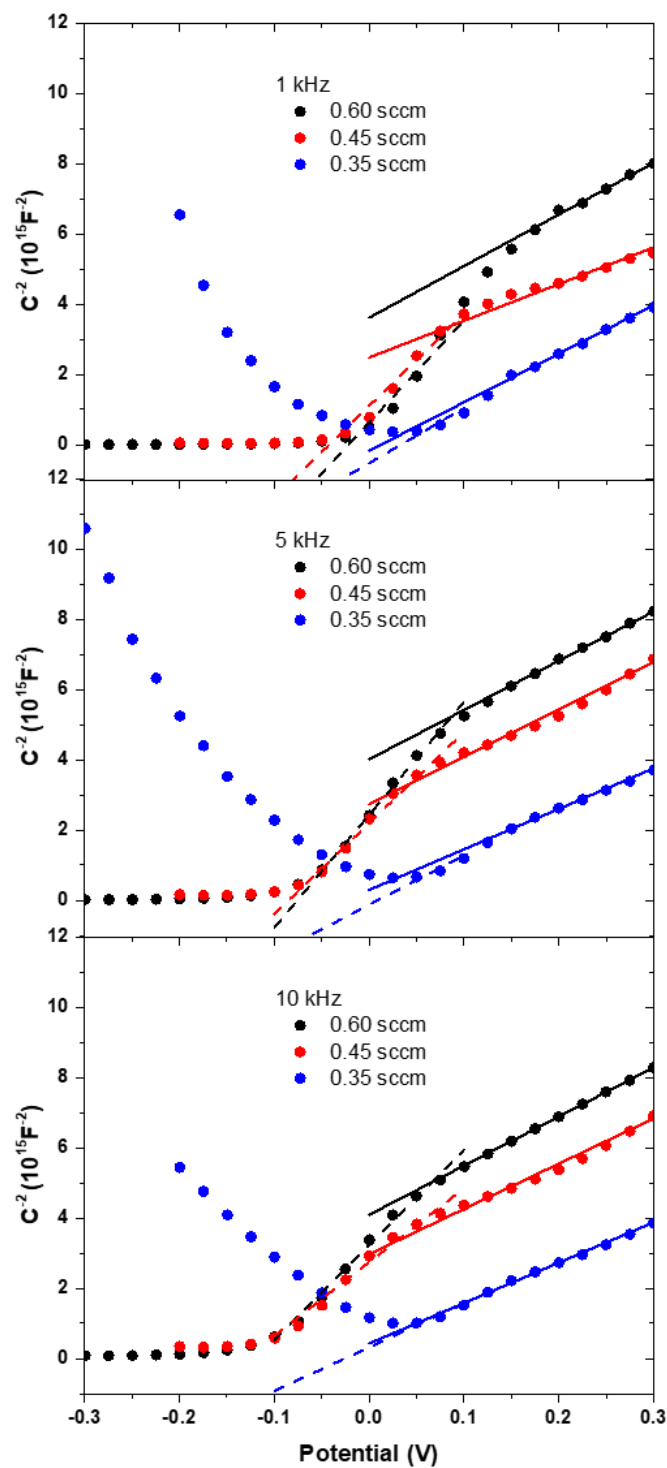


Fig. S13. Solid state Mott-Schottky (MS) plot for n -Si/TiO_x (50 nm)/Ni photoanodes fabricated with each oxygen flow obtained in air. Linear fitting results related to the n -Si substrate and TiO_x overlayer are shown as solid and dashed lines, respectively.

Table S3. MS parameters of *n*-Si photoanodes with protective TiO_x films deposited at 0.60, 0.45, and 0.35 *sccm*, measured at 1 and 10 kHz AC modulation. Previously reported dielectric constant of Si and a-TiO₂ was used for the calculation of carrier density.

Photoanode Component (AC modulation = 1 kHz)	Mott-Schottky parameters	Oxygen Flow (<i>sccm</i>)		
		0.35	0.45	0.60
<i>n</i> -Si $\epsilon = 12$	V_{fb} (V)	0.012	-0.237	-0.246
TiO _x $\epsilon = 33$	Slope ($10^{15}F^{-2}V^{-1}$)	15.66	26.20	29.07

Photoanode Component (AC modulation = 10 kHz)	Mott-Schottky parameters	Oxygen Flow (<i>sccm</i>)		
		0.35	0.45	0.60
<i>n</i> -Si $\epsilon = 12$	V_{fb} (V)	-0.037	-0.231	-0.293
TiO _x $\epsilon = 33$	Slope ($10^{15}F^{-2}V^{-1}$)	12.43	21.02	27.10

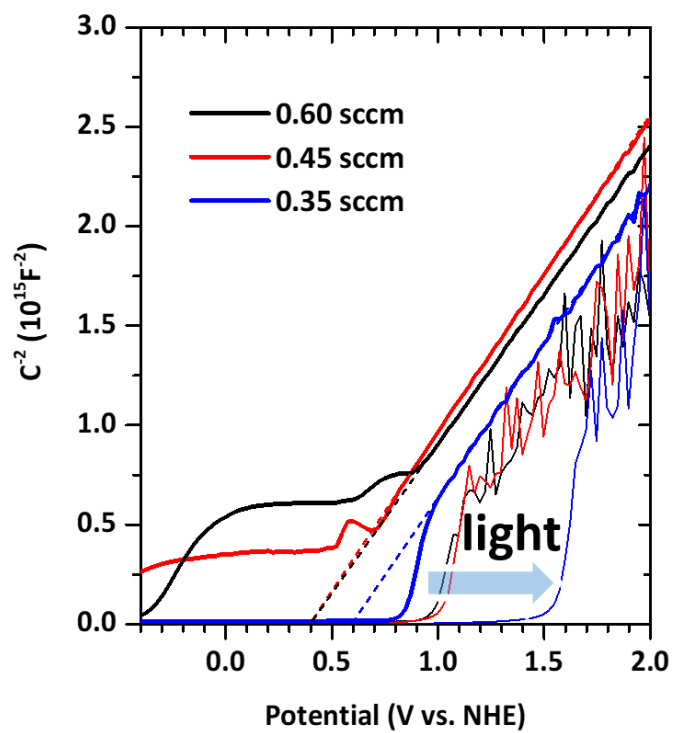


Fig. S14. MS data for *n*-Si/TiO_x (50 nm)/Ni photoanodes in 1 M KOH measured in the dark (thick lines) and under 1-sun illumination (thin lines). The shift in the capacitance response relates to the photo-generated carriers.

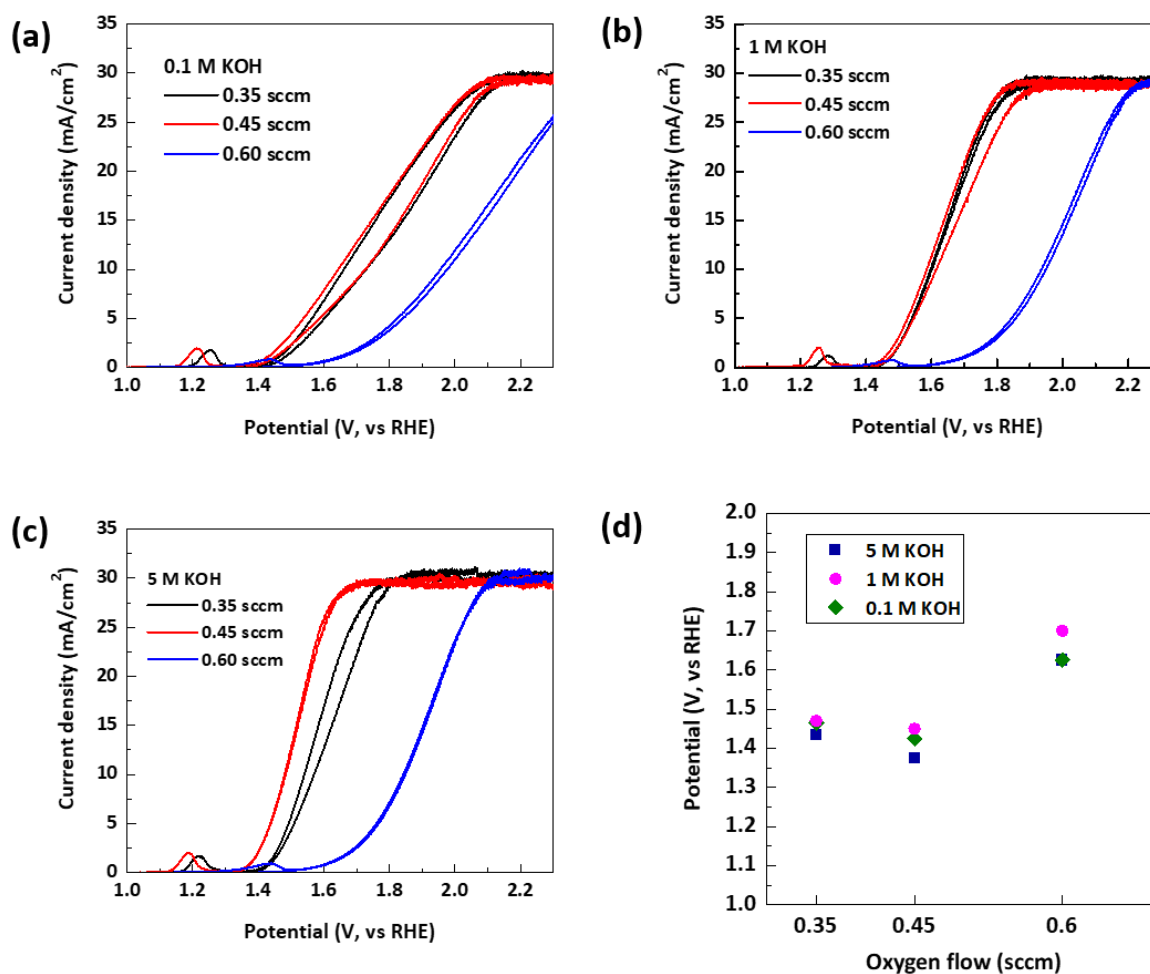


Fig. S15. Stirred cyclic voltammetry of *n*-Si/TiO_x (10 nm)/Ni photoanodes under (a) 0.1 M, (b) 1 M, and (c) 5 M KOH electrolyte. (d) Plot of overpotential at 1 mA/cm² of each photoanode measured at the different electrolyte concentration.

In order to explore the universality of proposed mechanism, the PEC activity of 10 nm TiO_x protected *n*-Si/*sub*-TiO_x/Ni photoanode was monitored under 0.1 M, 1 M, and 5 M KOH electrolyte. Same with the results performed in 1 M KOH (Fig. 1c and 2b), the 0.45 sccm photoanode showed the best water-splitting activity (0.45 > 0.35 > 0.6 sccm). It can be concluded that the defect density of TiO_x layer is directly related to the water-splitting activity of *n*-Si photoanode. This result shows that electrolyte with lower ion concentration induces the higher overpotential as well as the decreased squareness in J-V curve. Although the slight changes in J-V curves were observed, the same tendency of PEC activity depending on defect density of TiO_x was observed for all electrolyte concentrations. It supports that the proposed mechanism is also valid in diluted (0.1 M) and concentrated (5 M) electrolyte.

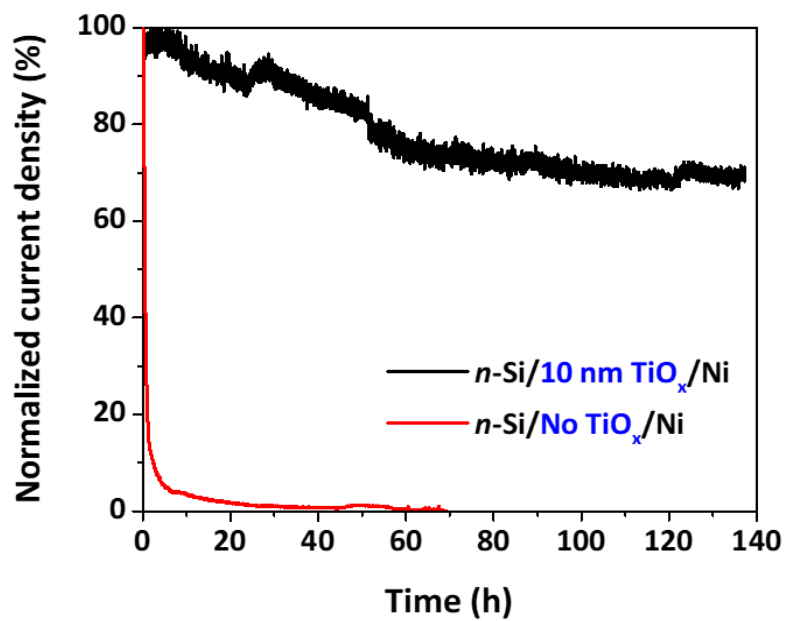


Fig. S16. Chronoamperometry of *n*-Si photoanode with (black) and without (red) 10 nm TiO_x (0.45 *sccm*) protection layer during water oxidation in 1.0 M KOH(*aq*) under simulated 1-sun illumination ($V=2.0$ V vs RHE).

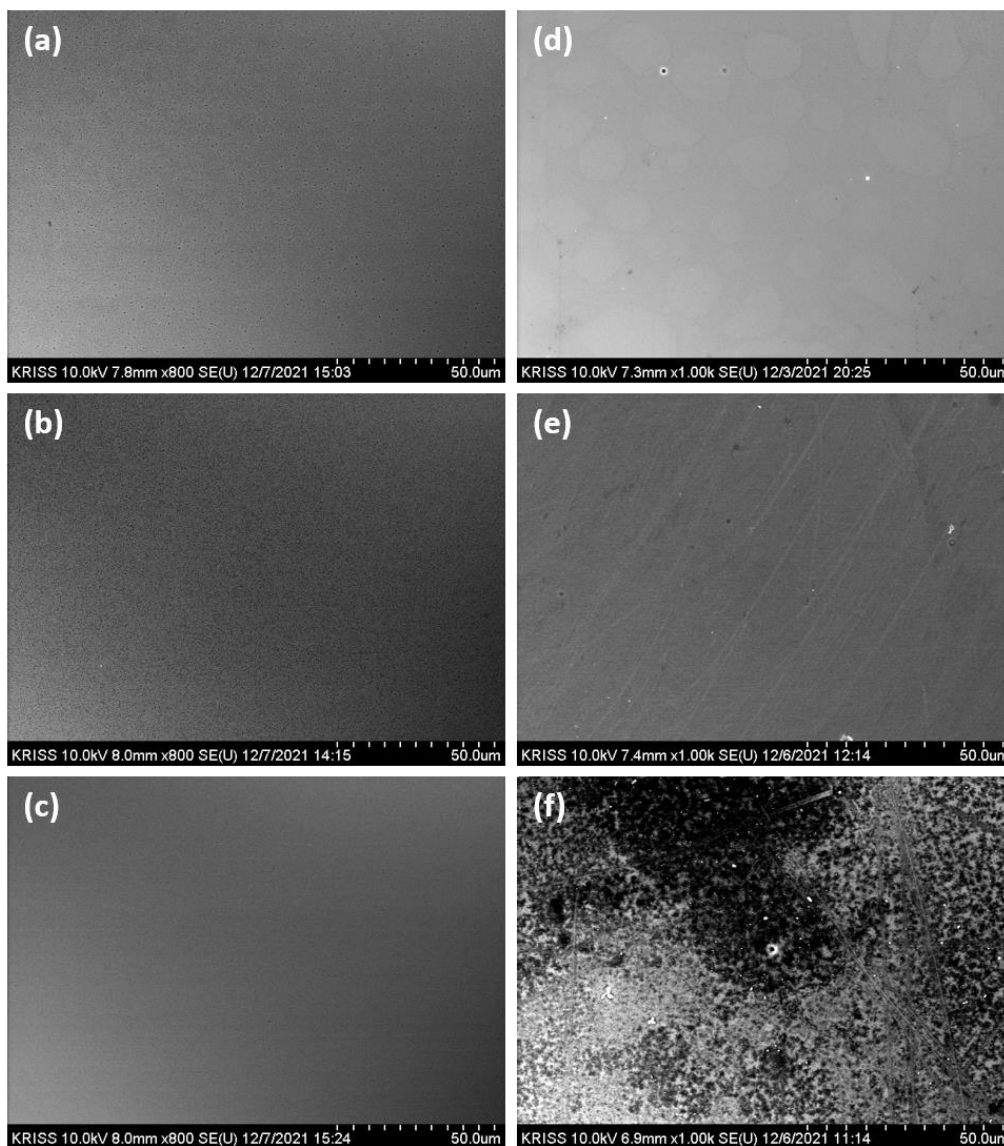


Fig. S17. Top-view SEM images of pristine *n*-Si photoanode protected by 50 nm of TiO_x deposited in (a) 0.35, (b) 0.45, and (c) 0.60 *sccm* of O₂ flow. 3.3 nm-thick Ni cocatalyst was deposited onto TiO_x layer all on *n*-Si. (d-f) Top-view SEM images of various *n*-Si/TiO_x/Ni photoanodes after the chronoamperometry depicted in Fig. 6. The O₂ flow for the three TiO_x layers is (d) 0.35, (e) 0.45 and (f) 0.60 *sccm*.

As increasing the O₂ flow, the PEC reaction-induced surface damage is more clearly visible as demonstrated in Figs. S17d-f. The 0.60 *sccm* sample (Fig. S17f) shows uncountable surface scratches and pin holes, but the 0.35 *sccm* sample surface exhibits the least damaged. The surface morphology observed in the SEM images directly correlates with the chronoamperometry result depicted in Fig. 6.

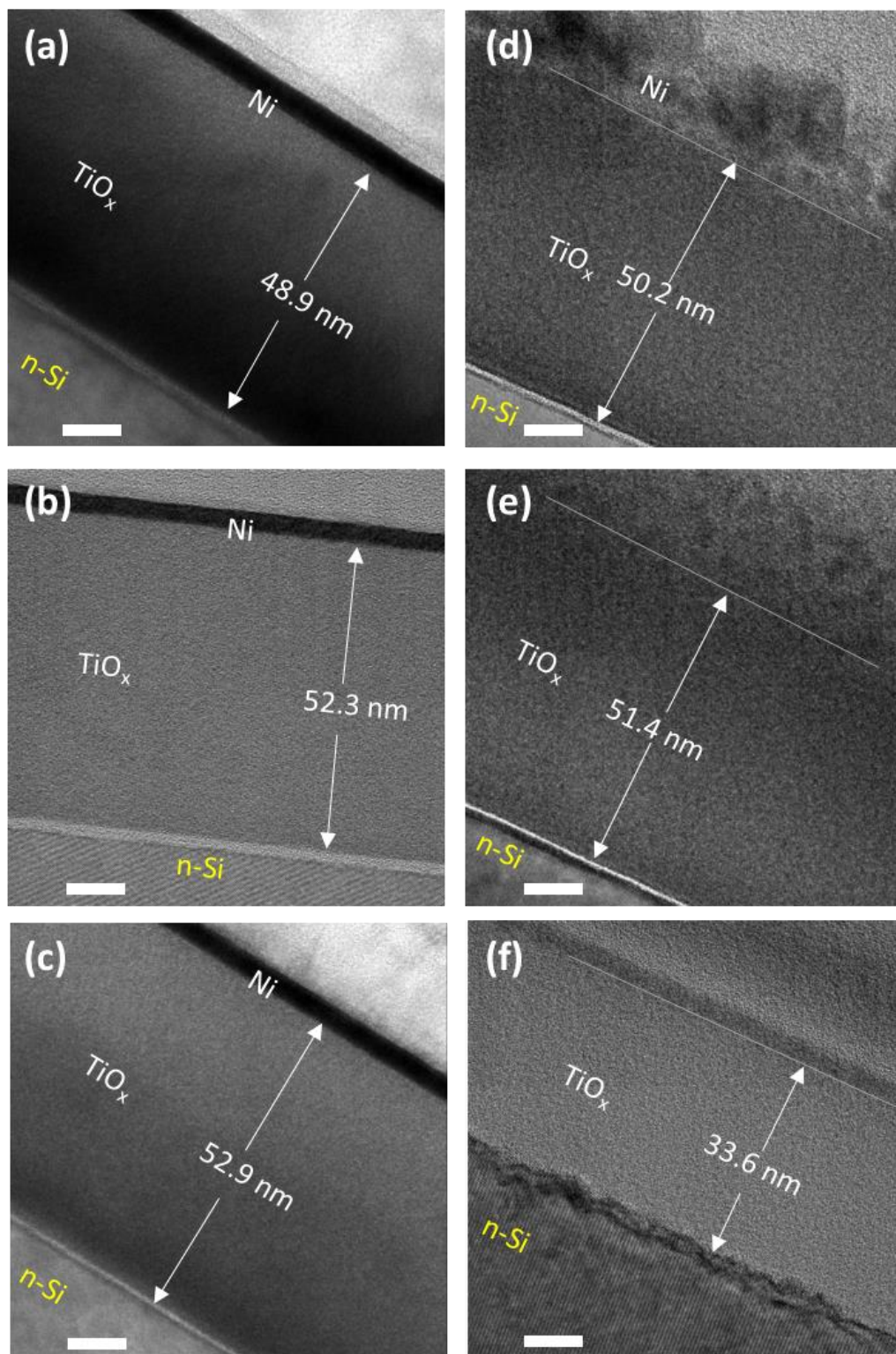


Fig. S18. Cross-sectional TEM images of pristine n-Si photoanode protected by 50 nm of TiO_x deposited in (a) 0.35, (b) 0.45, and (c) 0.60 *sccm* of O₂ flow. Approximately 3.3 nm-thick Ni cocatalyst was deposited onto TiO_x layer all on n-Si. (d-f) Cross-sectional TEM images of various n-Si/TiO_x/Ni photoanodes after the chronoamperometry depicted in Fig. 6. The O₂ flow for the three TiO_x layers is (d) 0.35, (e) 0.45 and (f) 0.60 *sccm*. The length of scale bar is 10 nm.

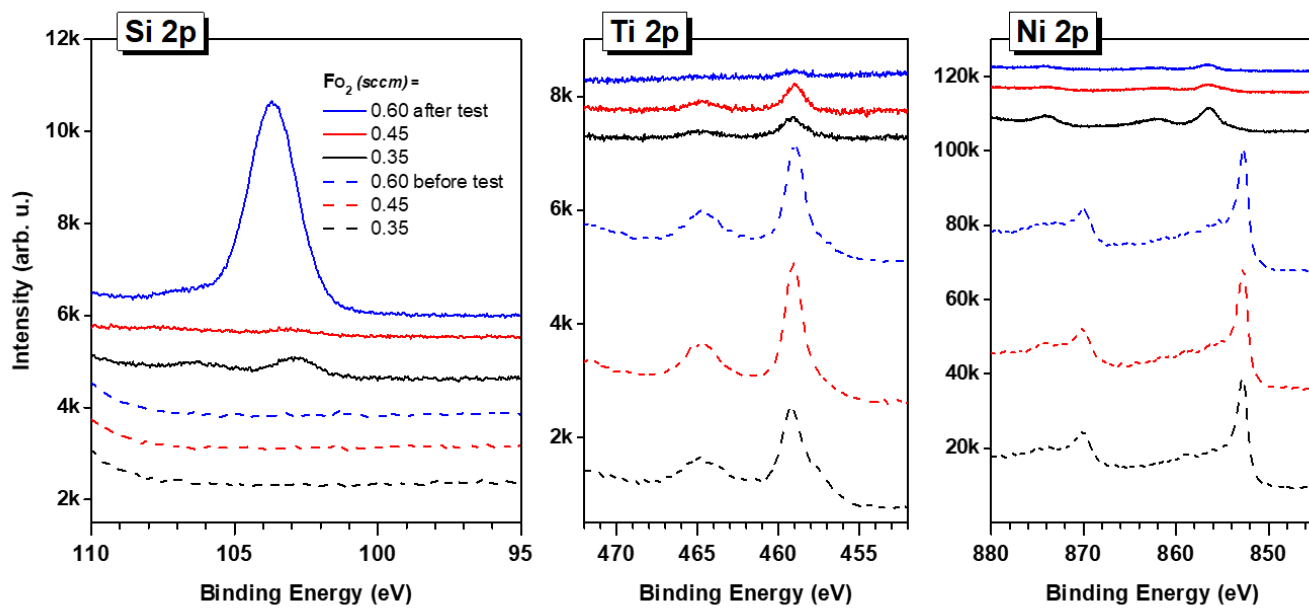


Fig. S19. Si 2p, Ti 2p and Ni 2p core level of n-Si/TiO_x/Ni photoanodes deposited in 0.35, 0.45, and 0.60 *sccm* of O₂ flow before (dashed line) and after (solid line) the stability test depicted in Fig. 6.

Reference

1. G. Tompsett, G. Bowmaker, R. Cooney, J. Metson, K. Rodgers and J. Seakins, *J. Raman Spectrosc.*, 1995, **26**, 57-62.
2. D. Zhigunov, G. Kamaev, P. Kashkarov and V. Volodin, *Appl. Phys. Lett.*, 2018, **113**, 023101.
3. P. A. Temple and C. Hathaway, *Phys. Rev. B*, 1973, **7**, 3685.
4. B. D. Piercy, C. Z. Leng and M. D. Losego, *J. Vac. Sci. Technol. A*, 2017, **35**, 03E107.
5. D. Mergel, D. Buschendorf, S. Eggert, R. Grammes and B. Samset, *Thin Solid Films*, 2000, **371**, 218-224.
6. O. Anderson, C. R. Ottermann, R. Kuschnereit, P. Hess and K. Bange, *Fresenius J. Anal. Chem.*, 1997, **358**, 315-318.
7. T. Zhai, S. Xie, M. Yu, P. Fang, C. Liang, X. Lu and Y. Tong, *Nano Energy*, 2014, **8**, 255-263.